

Structural insights into cardiolipin stabilization of yeast respiratory supercomplexes revealed byCryo-EM

4 Corey F. Hryc¹

McGovern Medical School

Venkata K. P. S. Mallampalli

McGovern Medical School

Evgeniy I. Bovshik

McGovern Medical School

Stavros Azinas

McGovern Medical School

5 Guizhen Fan

McGovern Medical School

Irina I. Serysheva

McGovern Medical School

Genevieve C. Sparagna

University of Colorado at Boulder

Matthew L. Baker

McGovern Medical School

Eugenia Mileykovskaya (✉ Eugenia.Mileykovskaya@uth.tmc.edu)

McGovern Medical School

William Dowhan (✉ william.dowhan@uth.tmc.edu)

McGovern Medical School

Research Article

Keywords: cardiolipin, phosphatidylglycerol, respiratory supercomplexes, mitochondria, yeast, cryo-EM

Posted Date: September 2nd, 2022

DOI: <https://doi.org/10.21203/rs.3.rs-2015065/v1>

License: © ⓘ This work is licensed under a Creative Commons Attribution 4.0 International License.

[Read Full License](#)

1 Structural insights into cardiolipin stabilization of yeast respiratory supercomplexes revealed by
2 Cryo-EM

3

4 Corey F. Hryc^{1,4}, Venkata K. P. S. Mallampalli^{1,2,4}, Evgeniy I. Bovshik^{1,4}, Stavros Azinas^{1,4},
5 Guizhen Fan^{1,2,4}, Irina I. Serysheva^{1,2,3,4}, Genevieve C. Sparagna⁵, Matthew L. Baker^{1,2,4}, Eugenia
6 Mileykovskaya^{1,4,*}, William Dowhan^{1,2,3,4,*}

7

8 ¹Department of Biochemistry and Molecular Biology, ²Structural Biology Imaging Center, and
9 ³Center for Membrane Biology, ⁴McGovern Medical School, The University of Texas Health
10 Science Center Houston, Texas 77030 and the ⁵Department of Integrative Physiology, University
11 of Colorado at Boulder, Boulder, Colorado 80309

12

13

14

Abstract

15

16 Cardiolipin is a hallmark phospholipid of mitochondrial membranes. Despite established
17 significance of cardiolipin in supporting respiratory supercomplex organization, a mechanistic
18 understanding of this lipid-protein interaction is still lacking. To address the essential role of
19 cardiolipin in supercomplex organization, we determined cryo-EM structures of a wild-type
20 supercomplex (IV₁III₂IV₁) and a supercomplex (III₂IV₁) isolated from a cardiolipin-lacking
21 *Saccharomyces cerevisiae* mutant at 3.2-Å and 3.3-Å resolution, respectively.
22 Phosphatidylglycerol is located in the III₂IV₁ supercomplex at similar positions as cardiolipin in the
23 wild-type supercomplex. Lipid-protein interactions in the latter are different from that observed for
24 the former that conceivably underlies the reduced stability of supercomplexes in mutant
25 mitochondria. Our studies provide evidence that anionic phospholipids appear to nucleate a
26 phospholipid domain at the interface between the individual complexes, which may contribute to
27 supercomplex stability. Destabilization of supercomplex formation by phosphatidylglycerol has
28 significant implications for Barth Syndrome patients where mitochondrial phosphatidylglycerol
29 levels are significantly elevated.

30

31 The anionic phospholipid cardiolipin (CL) is uniquely localized to mitochondria, where it
32 constitutes approximately 20% of the inner mitochondrial membrane (IMM) phospholipid
33 throughout nature. CL is distinguished from other phospholipids by its unique dimeric structure
34 containing two phosphates, four fatty acids and a free hydroxyl at the 2-position of the glycerol
35 linking the two phosphatidyl groups. This unique dimeric structure makes CL ideal for supporting
36 the organization of individual protein subunits into multi-subunit complexes, as well as individual
37 complexes into supercomplex (SC) molecular machines, such as the mitochondrial respirasome.
38 Crystal structures of the individual respirasome complexes with CL integral to the structures
39 demonstrate its ability to link subunits within individual complexes ¹. However, these are stable
40 structures, which do not undergo dissociation/association of the subunits from the larger
41 complexes.

42 The current model of the *Saccharomyces cerevisiae* mitochondrial respiratory chain involves
43 the shuttling of electrons via mobile carriers (coenzyme Q (CoQ) and cytochrome *c* (Cyt *c*))
44 between either individual free respiratory complexes or individual complexes organized into
45 higher order SCs ²⁻⁸. The *S. cerevisiae* respiratory SC is composed of complexes III₂ (CIII, dimer
46 of cytochrome *bc*₁) and IV (CIV, Cyt *c* oxidase) with CIII flanked on each side by CIV in the core
47 SC (IV₁III₂IV₁) ⁹⁻¹¹. Our original discovery of an *in vivo* requirement for CL for formation of the SC
48 tetramer (III₂IV₂) in yeast mitochondria ^{12,13}, as well as a requirement for reconstituting the SC
49 from individual complexes *in vitro* ¹⁴ is supported by several reports using electron cryomicroscopy
50 (cryo-EM), which have verified CL molecules at the interface between CIII and CIV in yeast ^{10,15,16}
51 and mammalian systems ¹⁷⁻¹⁹. CL may provide a dynamic flexible link between individual
52 complexes within SCs, which allows association/dissociation of individual complexes into/from
53 SC structures that may be required to regulate energy production in response to varying
54 physiological conditions ²⁰. Lower CL levels are associated with reduced formation of SCs with
55 an increase in individual complexes in neurodegenerative diseases ²¹, ischemia followed by
56 reperfusion ^{22,23}, induction of apoptosis ²⁴⁻²⁶, heart failure ²⁷⁻²⁹, cancer ³⁰, Barth Syndrome ³¹,
57 hypothyroidism ³², obesity ³³ and aging ³⁴. A presumed advantage in SC formation is bringing
58 active sites of CIII and CIV in close proximity to each other to facilitate Cyt *c* shuttling of electrons
59 ^{16,35}. In addition, Cyt *c* binding to the SC is envisioned to restrict it to 2D diffusion between the
60 above active sites providing a presumed kinetic advantage ³⁵. In spite of the correlation between
61 the above disease states and reduced CL levels in mammalian systems and compromised
62 respiratory function in yeast mutants lacking CL ^{12,36,37}, there is still considerable debate as to the
63 precise role or advantage SC formation has in cell function.

64 The requirement of CL for SC formation is still not completely resolved. Digitonin extracts of

65 wild type (WT) yeast mitochondria when displayed by Blue Native (BN)-PAGE reveals almost
66 exclusively a tetrameric SC (III₂IV₂)¹². However, digitonin extracts from mutants lacking CL (*crd1*Δ
67 mutant) still show significant levels of a trimeric (III₂IV₁) SC and low amounts of the tetrameric SC
68 with large amounts of free CIV and CIII depending on the PAGE system employed³⁸. Therefore,
69 higher order SC formation still occurs in the absence of CL, but the stability of these complexes
70 appears to be significantly reduced, which has minimized the importance of a CL or lipid
71 requirement in SC formation in favor of protein-protein interactions being the primary basis for SC
72 formation¹. However, in these yeast mutants anionic CL is replaced by a comparable amount of
73 its precursor anionic phosphatidylglycerol (PG)³⁶, which contains only one phosphate and two
74 fatty acids. Surprisingly, individual complexes with structurally required internal CLs are still
75 functional^{13,38}, although SC stability and whole respiratory chain kinetic properties are altered¹³.

76 To date no high-resolution structural information has been presented for respiratory
77 complexes or SCs isolated from yeast mutants lacking CL or from mammalian mitochondria under
78 conditions where CL levels are reduced with increased levels of PG³⁹ to determine if and where
79 PG might substitute for CL in either individual complexes or SCs. To further our understanding of
80 the lipid requirement for SC formation, we report the cryo-EM maps and molecular models of the
81 WT yeast SC (III₂IV₂) solved to 3.2 Å resolution (Fig. 1 a1 and b1), and the trimeric SC (III₂IV₁)
82 isolated from a *crd1*Δ mutant solved to 3.3 Å resolution (Fig. 1 a2 and b2). These two structures
83 provide the basis to study positioning of the anionic phospholipids CL and PG and their
84 involvement in SC stabilization.

85

86 **Results**

87 **Structure of the WT yeast III₂IV₂ SC.** For purification (See Methods) of the SC extracted by
88 digitonin from the WT strain, we used the sucrose gradient purification method described in
89 detail in our previous paper⁹. The SC obtained by this method is active and demonstrates a low
90 level of the ubiquinol oxidase activity without any addition of Cyt *c*. A low level of Cyt *c* bound to
91 SC was detected by Western blot with antibody to Cyt *c*⁹.

92 The cryo-EM map displayed a global resolution of 3.2 Å (for data collection and image
93 processing see Methods, Supplementary Table 1 and Supplementary Fig. 1) and revealed CIII
94 flanked by CIV monomers on each side (Fig.1 a1), which is in line with previously published
95 structures^{10,11,15,35}. Local resolution of the final density map shows that the central part of the
96 map, which includes CIII, is better resolved than the CIV monomers (Supplementary Fig. 1f),
97 consistent with the suggested dynamic character of CIV^{10,11,15,35}. The reconstruction also revealed
98 that one CIV was better resolved, and thus, we denoted this side as the reference-side, with the

Figure 1.

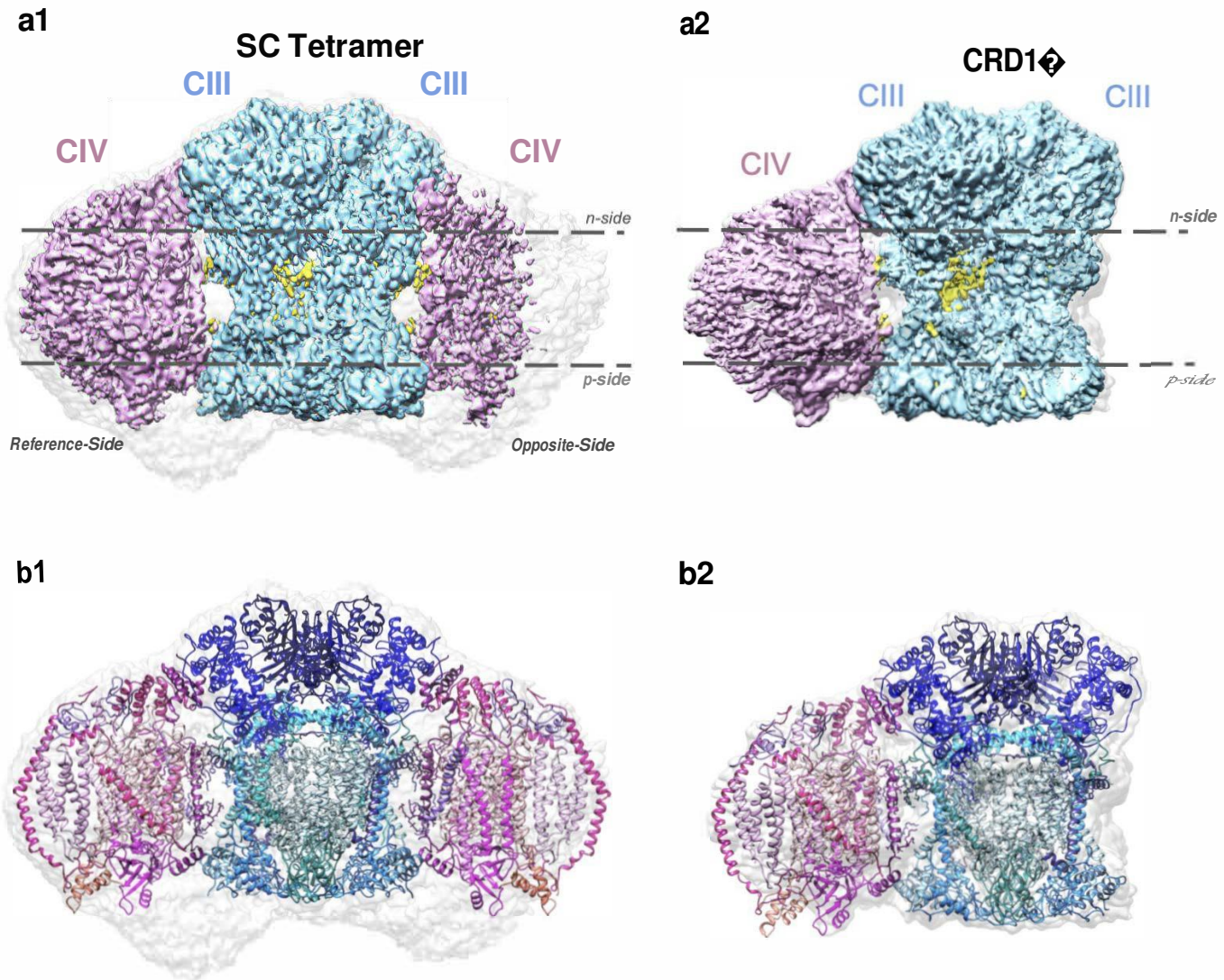


Figure 1. Cryo-EM density map and model for WT SC (left) and *crd1* Δ mutant SC (right). The segmented cryo-EM density maps for WT SC tetramer (1a) and *crd1* Δ mutant SC trimer (2a) are shown with colors distinguishing CIII (light blue), CIV (pink), ligands and cofactors (yellow). The grey regions of the density maps show low-threshold density areas, which maybe noise, detergent and/or potential structured regions, albeit with flexibility. Models were generated (as discussed in methods) for WT SC tetramer (1b) and *crd1* Δ mutant SC trimer (2b). A ribbon representation of CIII subunits is displayed in shades of blue, and CIV subunits are displayed in shades of pink.

99 weaker resolved side being denoted as the opposite-side. Our subsequent findings focus on the
100 reference-side of the map, unless otherwise noted. For construction of the WT SC tetramer model
101 IV₁III₂IV₁ (Fig. 1 b1; Supplementary Fig. 2), we used the previously reported structure of the SC
102 from *S. cerevisiae* (pdb: 6HU9)¹⁰. While the 6HU9 model generally fit the density, additional rigid-
103 body adjustments and local refinements were necessary. The adjusted model was then refined
104 with ligand restraints in Phenix⁴⁰. See the detailed description of the model building in Methods
105 and Supplementary Table 2, and subunit/chain names in Supplementary Table 3.

106 Although our model of the WT SC (Fig. 1 b1 and Supplementary Fig. 2 a and b) is in close
107 agreement with published models, examination of our map revealed differences with the
108 published results. Specifically, a difference map revealed discrete densities within CIII and at the
109 interface of CIII and CIV in our reconstruction that were not seen in the previously published
110 structure (pdb ID 6HU9)¹⁰. To model these unknown densities, previously resolved yeast SCs
111 and CIII (pdb ID: 6YMX¹⁶, 1KB9⁴¹, 3CX5⁴², 6Q9E,⁴³ 6GIQ¹¹) were fit in the map. We identified
112 an extra density located at the ubiquinone (UQ6) position of 6YMX (C406) (Q_i - inside site; also
113 known as Q_N negative site). Further analysis of the difference map revealed strong excess density
114 at the location of SMA (stigmatelin) seen in 1KB9; however, our sample preparation did not
115 include this inhibitor. This density was observed on both the reference-side and opposite-side of
116 the complex. UQ6 was modeled at those locations (Q_o - outside sites, also known as Q_P-positive
117 sites). Since the reference-side UQ6 lacked strong tail density, the model was truncated to match
118 the density. In total, four UQ6 ligands were placed into the map, two in each monomer of CIII,
119 with one UQ6 having a large break in the tail density (Fig. 2). To the best of our knowledge, this
120 is the first time the structure of a *S. cerevisiae* respiratory SC was obtained in which not only Q_i
121 sites but also both Q_o sites of CIII are occupied by UQ6^{10,11,35}.

122 In our structure, UQ6 interacts with His181 of the head domain of Rip1 (Rieske protein) in the
123 Q_o site of the opposite-side monomer of CIII, which interacts with the more poorly resolved
124 CIV monomer. The Q_o site on the reference-side of CIII, which interacts with the reference CIV,
125 lacks a strong UQ6 tail density, which might be an indication of increased UQ6 flexibility at this
126 site. The position of the Rip1 flexible domain on both sides is rather similar to its position in the
127 3CX5 crystal structure of CIII (*b* position)⁴² than to positions of this domain in the 6HU9 or 6YMX
128 SC structures (intermediate position, between *b* and *c* positions^{10,16} Supplementary Fig. 3).
129 Further studies of the SC purified by sucrose gradient centrifugation and its red-ox state are
130 required to provide a detailed explanation of this arrangement.

131

132

Figure 2.

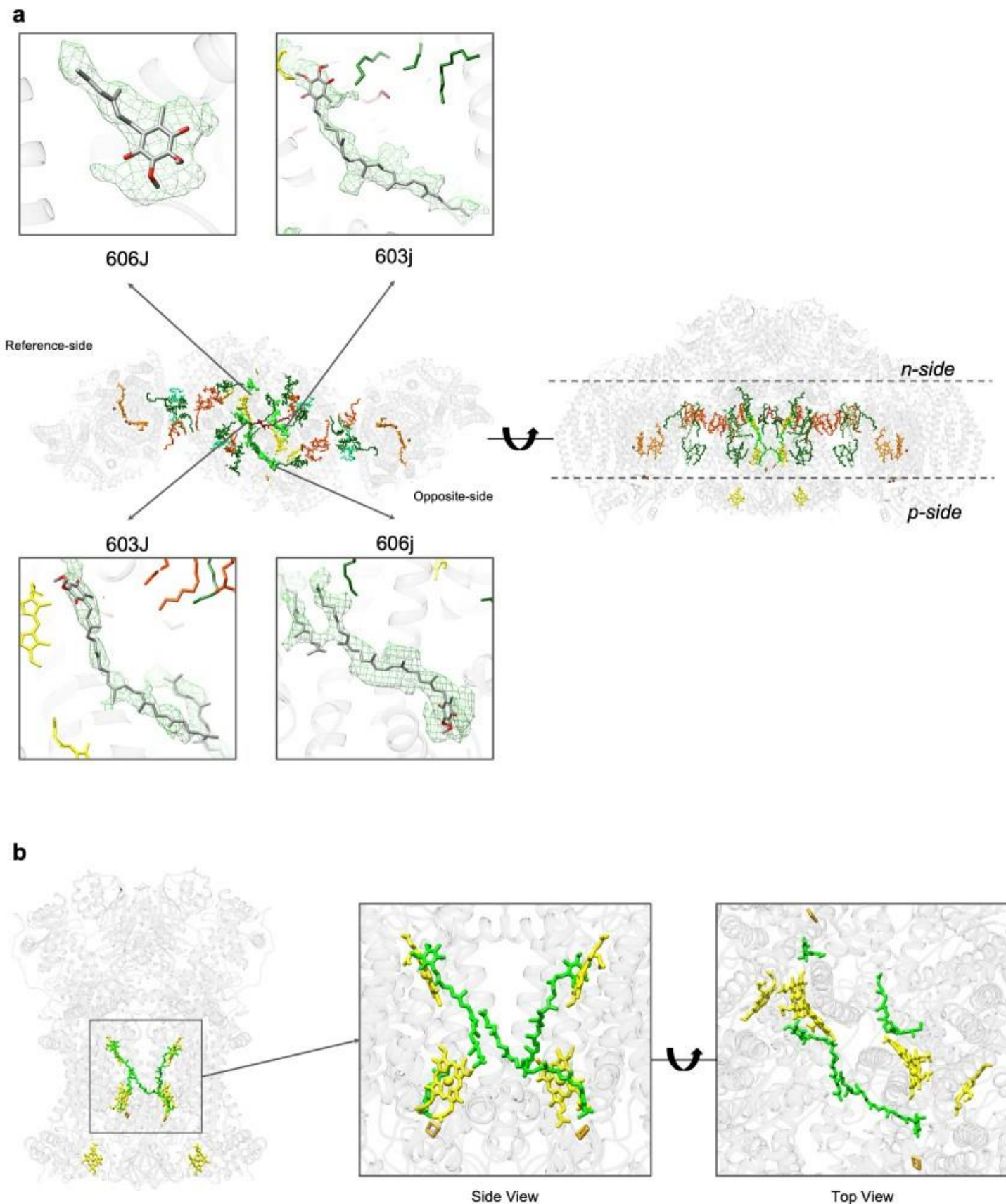


Figure 2. Gallery of UQ6 ligands for the WT SC. a The model is shown with isolated density for each of the four UQ6s identified in the density map. The truncated UQ6 606J is on the reference-side of CIV and the p-side of the CIII complex. b UQ6 (shown in green atom representation) position is highlighted with respect to CIII (grey). In addition to FES (gold) and Hemes bH and bL (yellow) are shown.

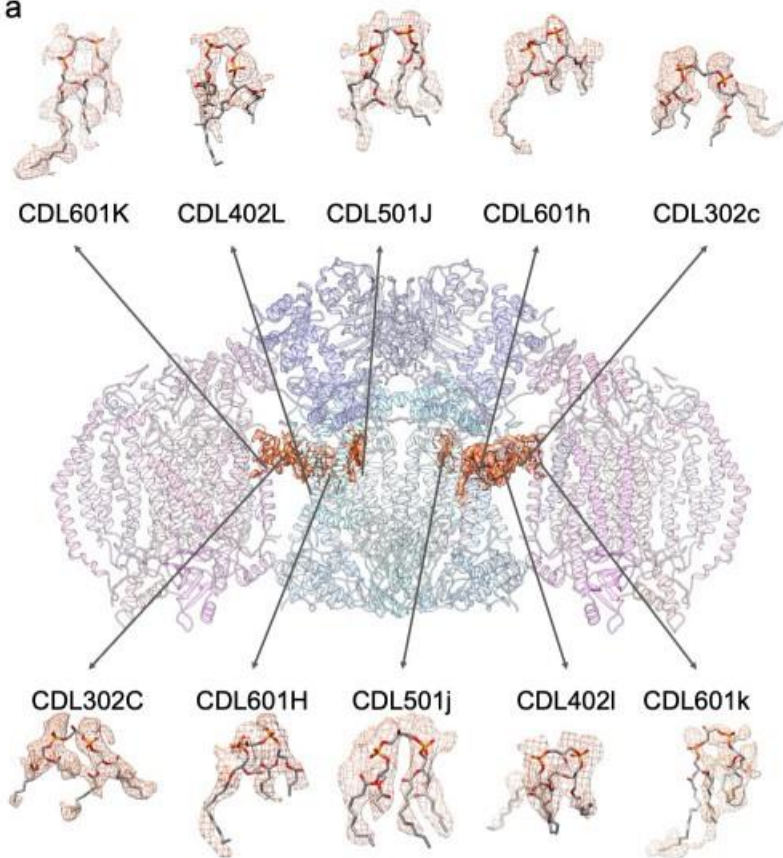
133 Finally, our density map at the 2-fold of CIII does not accommodate UQ6, which was modeled
134 at this position in 6HU9, Various attempts to fit this density were made based on previously known
135 SCs. CN5 (CL) from 6YMX was the best fit for this density, thus, it was modeled at this site
136 (Supplementary Fig. 2 a and b).

137
138 **Localizarion of Cardiolipin in the WT SC structue.** Non-protein densities in our WT SC
139 structure were observed at the locations of CL (Fig. 3a, CDL=CL) in the previously solved cryo-
140 EM structures of the yeast SC ^{10,11,15,35}. Thus, we assigned these densities to CL molecules (see
141 Methods). The hydrophilic headgroups of these CLs interact with amino acid side chains through
142 hydrogen bonding and/or salt bridges (Fig. 3b). Two CL molecules (CDL601K/k and CDL302C/c)
143 at each CIII/CIV interface and one CL (CDL501J/j) within each of the monomers of CIII were fit
144 into these densities (Fig. 3a) allowing us to assign possible interactions of the CLs with the SC
145 proteins and other phospholipids. One phosphate residue of CDL501J (Fig. 3b and
146 Supplementary Fig. 4a) is in close proximity to Arg4 of Cob and His345 of Cor1 within CIII. Only
147 CDL601K (Fig 3b and Supplementary Fig. 5b) appears to interact with both CIII and CIV through
148 phosphate moities and Lys35 of Qcr8 in CIII and Lys487 of Cox1 in CIV, respectively. CDL302C
149 (Fig. 3b) is in close proximity to CDL601K, and its phosphates appear to interact with Lys44 and
150 Lys51 of Rip1 on the surface of CIII at the interface with CIV (Supplementary Fig. 5a). A density
151 for CDL402L (Fig. 3a and b) in which one phosphate is in close association with Lys288 of Cyt1
152 and Tyr28 of Cob in CIII was also observed (Supplementary Fig. 6a). CDL601H (Supplementary
153 Fig. 6b) fit a density also in association with CIII in which one phosphate appears to interact with
154 His85 in Qcr7, and the other phosphate appears to interact with Arg8 of Qcr8. Interestingly,
155 CDL302C is in close proximity to both CDL601K and CDL402L with the latter in close proximity
156 to CDL601H (Supplementary Fig. 5 and 6). These CLs appear to form a hydrophobic domain that
157 may enhance binding between CIII and CIV by stabilizing CL at the interface. CDL402L like CN3
158 (CL), previously identified by X-ray crystallography ^{1,41}, lies in a groove of CIII and neutralizes
159 positively charged residues of subunit Cyt1 near CDL402L. Although this area of the CIII surface
160 where CDL402L and CDL601H are located is near the CIII/CIV interface, it does not directly face
161 the surface of CIV.

162
163 **Structure of the III₂IV₁ trimeric SC isolated from the *crd1*Δ mutant.**
164 To address whether CL is critical for SC formation, we performed single-particle cryo-EM analysis
165 of the trimeric SC purified from *crd1*Δ cells. Using mass spectral analysis (see Methods), we
166 confirmed that the yeast *crd1*Δ mutant contains the immediate precursor of CL,

Figure 3.

a



b

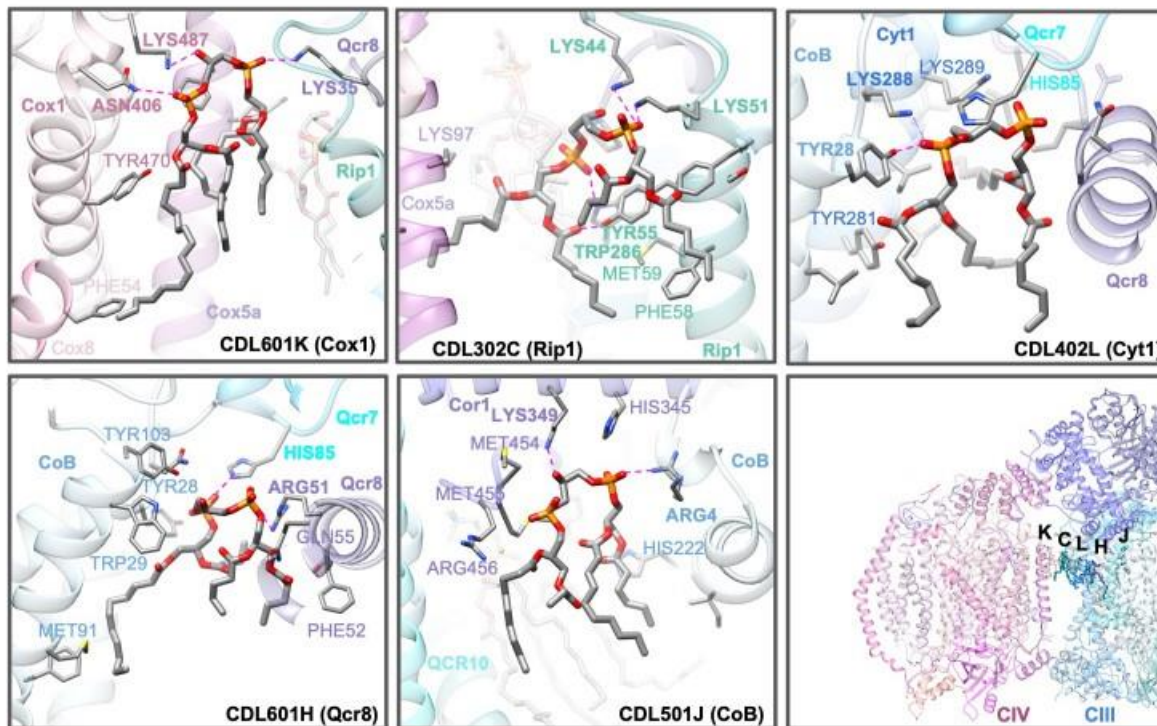


Figure 3. Gallery of CDL ligands in the WT SC structure. a The model is shown with isolated density for each of the CDL ligands identified in the density map. A zone equivalent to the resolution (3.2Å) was used to isolate the density map corresponding to the model. b CDL potential interactions with neighboring subunits of the SC tetramer SC. The five CDLs are shown on the reference-side of the WT SC tetramer. Side chains within 4 Å of the focused CDL are displayed, with specific interactions being highlighted with bold side chain labels and a magenta dashed line. CDLs are labeled according to the chains' names, see Supplementary Table 3.

167 phosphatidylglycerol (PG), in place of CL. In *pgs1* Δ mutants that lack CL and PG, the nuclear
168 encoded components of CIII (Cob) and CIV (Cox1, Cox2 and Cox3) are no longer synthesized⁴⁴.
169 Therefore, no definitive structural requirement for PG in place of CL can be concluded from
170 genetic manipulation. To date, the possible replacement of CL with PG in individual respiratory
171 complexes and SCs has not been documented at the structural level. We purified the trimeric SC
172 from *crd1* Δ cells and carried out structural analysis by cryo-EM and model building. The III₂IV₁
173 trimeric SC with a Cox4-His tag was extracted by digitonin and purified using a His-Trap HP
174 column (see Methods). Grid preparation and cryo-EM data collection were similar to the WT
175 condition. Due to preferred orientation, additional images were collected at 30° tilt. Image
176 processing and final refinement using a tight mask around the SC resulted in 3.3 Å density map
177 (Fig. 1 a2). For details see Methods, Supplementary Table 1 and Supplementary Fig. 7 a-f.

178 To construct a model of the *crd1* Δ SC optimized protein subunits from CIII and CIV were
179 extracted from the WT model and fit independently into the *crd1* Δ trimeric SC 3.3 Å density map
180 with Chimera, followed by refinement in Phenix and COOT (see Methods and Supplementary
181 Table 2). There was no density in the region of the *crd1* Δ density map corresponding to the
182 position of the Qcr10 subunit of CIII in the WT SC density map; we assume that this subunit was
183 lost during purification. Unstable association of Qcr10 with CIII of *S. cerevisiae* has been
184 previously reported when CIII was purified for crystallographic analysis⁴⁵. All other subunits of
185 CIII and CIV in the mutant showed a similar organization and location as in the WT structure (see
186 Fig. 1 b2, Supplementary Fig. 8 and Supplementary Fig. 9; for subunits/chains names see
187 Supplementary Table 3). Densities for UQ6 were found only at Qi sites; Qo sites were empty.
188 Analysis of the cryo-EM density for Rip1 subunit of CIII showed that both the hinge region and
189 the head domain displayed weaker or less ordered density when compared to the WT. This
190 variation in density may indicate that the head domain of Rip1 in the *crd1* Δ CIII is flexible and
191 exists in a larger conformation space. This is consistent with the finding that this ectodomain is
192 stochastic when Q_o site is empty⁴⁶. In addition, there was no density at the position similar to CN5
193 (CL) in the WT structure. Importantly, the mutual orientation of the individual CIII and CIV from
194 the *crd1* Δ mutant was the same as in the WT SC (Fig. 1b2 and a2, Fig. 4a and Fig. 3a). This
195 allowed us to make a comparative analysis of the lipid positions in the mutant and WT structure
196 and focus on areas which in the WT SC were occupied by CL, including the interface between
197 CIII and CIV.

198

199 **Localization of phosphatidylglycerol (PG/PGT) in the *crd1* Δ SC.** As described in Methods, the
200 *crd1* Δ map was masked using the protein model to reveal unmodelled densities for cofactors and

Figure 4.

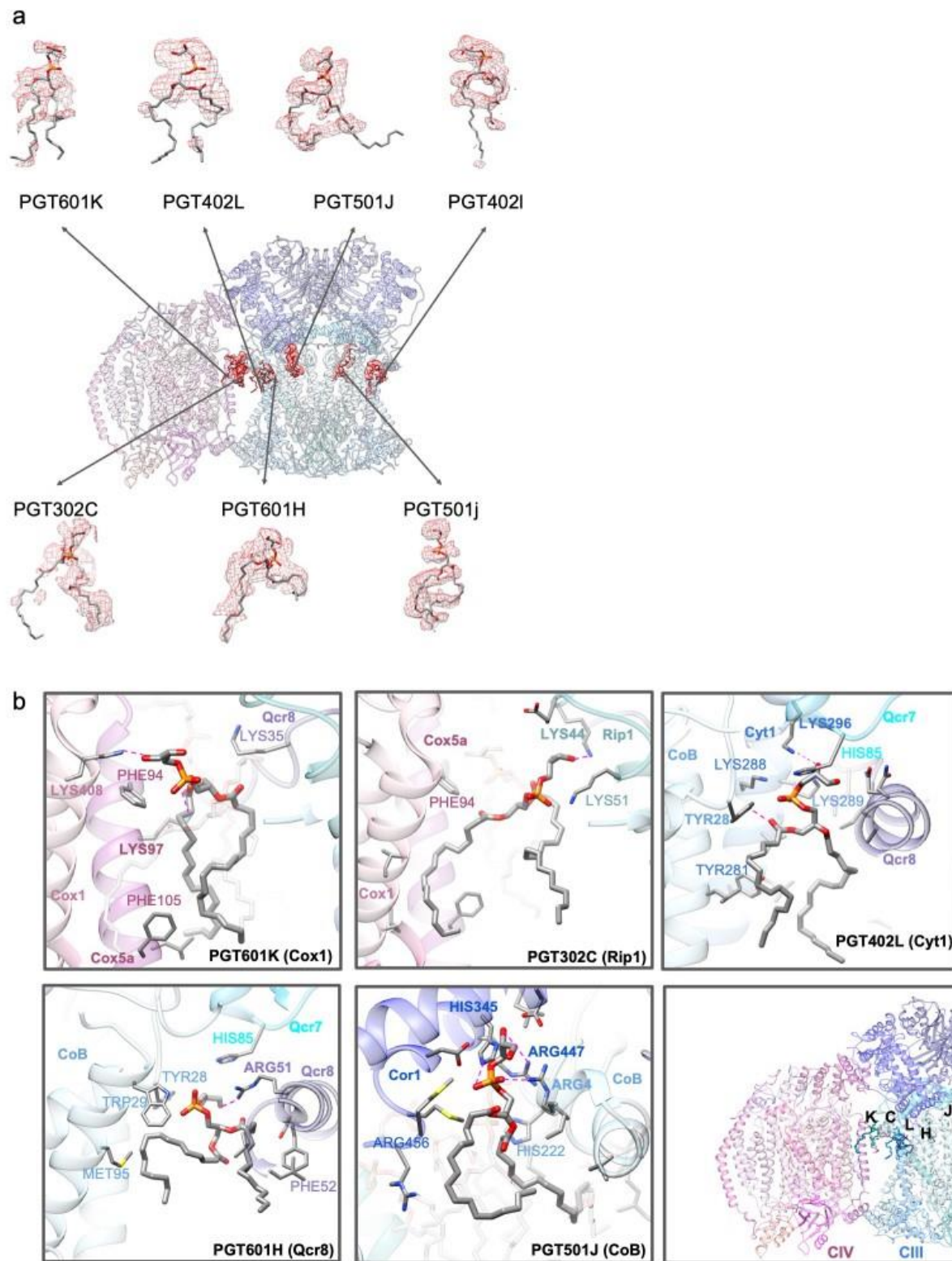


Figure 4. Gallery of PGT ligands in the *crd1* Δ SC structure. **a** The model is shown with isolated density for each of the PGT ligands identified in the density map. A zone equivalent to the resolution (3.3Å) was used to isolate the density map corresponding to the model. **b** PGT potential interactions with neighboring subunits of the *crd1* Δ SC. The five PGT ligands are shown on reference-side of the *crd1* Δ SC. Side chains within 4 Å of the focused PGT are displayed, with specific interactions being highlighted with bold side chain labels and a magenta dashed line. PGTs are labeled according to the chain names, see Supplementary Table 4.

201 lipids. Hemes, appropriate ligands (PEF (PE), PCF (PC)) and cofactors were then extracted from
202 the WT map and rigid body fit to the unmodeled parts of the *crd1Δ* density map. Importantly, the
203 positions corresponding to the CDL locations in the WT SC did have densities indicating the
204 presence of ligands. The density at these positions revealed two tails with one strong headgroup
205 as opposed to the four tails and two strong headgroups for CDL (Fig. 4a and b). This correlated
206 with positioning of the anionic phospholipid PGT (PG), which fit into the CDL positions. To further
207 test and confirm the fitting of PGT to these densities, PEF, PCF, and CDL were all fit into the
208 suggested PGT locations. One iteration of refinement was completed with the ligands in the PGT
209 density. Next, a calculated density map was computed for each of the ligand groups and the
210 threshold was set to be equivalent for each ligand group. Finally, the cross-correlation score was
211 computed for the six sites. PGT resulted in the highest average correlation (Supplementary Table
212 5).

213 PGT501J/j (Supplementary Fig. 4b) appears to replace the internal CLs in each monomer of
214 CIII surprisingly resulting in little noticeable structural changes for CIII. The one phosphate of this
215 PG is in close proximity to Arg4 of Cob as seen for CDL in this position. The remaining PGTs also
216 interact with similar regions of the SC as CDLs but with fewer or weaker interactions. The
217 headgroup of PGT302C (Supplementary Fig. 5c) lies near Lys44 of Rip1 (as does CDL302C) and
218 may interact with a hydroxyl of its glycerol headgroup rather than through the phosphate.
219 However, there is no interaction with Lys51 of Rip1 since PGT lacks a second phosphate.
220 PGT601K (Supplementary Fig. 5d) appears to only interact with CIV unlike CLD601K that
221 interacts with both CIII and CIV. Rather than stronger potential ionic interactions as observed for
222 CDL601K, only weaker interactions between a hydroxyl of the glycerol headgroup and Lys408 in
223 Cox1 of CIV and the carbonyl of the *sn*-1 fatty acid of PGT and Lys97 in Cox5a of CIV were
224 observed. The one phosphate of PGT402L (Supplementary Fig. 6c) is in close association with
225 Lys288 of Cyt1 and Tyr28 of Cob in CIII as observed for CLD402L. PGT601H (Supplementary
226 Fig. 6d) is in close association with Arg51 of Qcr8 in CIII but lacking a second phosphate does
227 not interact with His85 in Qcr7 of CIII. PGT601H and PGT402L like PGT302C and PGT601K are
228 in close proximity to each other, but unlike in the case of CL, PGT302C and PGT402L are close
229 (Fig. 4a) but appear to be further apart than CLs at this site (Supplementary Fig. 5 and 6).

230 The lack of significant formation of the tetrameric SC in the absence of CL may be due to
231 weaker interactions of PG with amino acids of both individual complexes, as well as no PG
232 molecules interacting with both CIII and CIV. The apparent weaker interactions of PG with the
233 individual complexes at the interface appears to be the basis for lack of tetrameric SC formation
234 under more stringent conditions of BN-PAGE. Reducing the amount of blue dye in the PAGE

235 system increases the amount of trimeric SC, with detection of some tetrameric SC in digitonin
236 extracts from *crd1Δ* mitochondria^{16,38}, which also supports the weaker interactions of PG within
237 the SC.

238

239 **Discussion**

240

241 The primary goal of this work was to understand the role of lipids in the organization of respiratory
242 SCs. Our reported structure for the tetrameric SC isolated from WT yeast mitochondria is in close
243 agreement with previously reported structures, except we were able to identify full occupancy of
244 the four UQ6 binding sites in CIII. CL molecules are identified within CIII and at the CIII/CIV
245 interface with one of the CLs interacting with both complexes.

246 The presence of tetrameric and trimeric SCs in mitochondrial extracts analyzed under mild
247 conditions from yeast lacking CL has been suggested to minimize the importance of lipids in SC
248 formation^{1,38}. Analysis of extracts from *crd1Δ* mitochondria under more stringent conditions shows
249 high levels of free CIII and CIV and the absence of tetrameric and trimeric SCs, which is not the
250 case for extracts from WT mitochondria¹². Our structural determination of the trimeric SC from
251 *crd1Δ* cells shows the presence of the anionic phospholipid PG. PG was resolved in the same
252 positively charged regions of the structure as CL. However, there were significant differences as
253 to which amino acids PG interacts with and none of the PGs formed interactions that bridge CIII
254 and CIV. These difference in the interaction of the individual complexes with the two anionic
255 phospholipids may explain the reduced stability of SCs when PG substitutes for CL, resulting in
256 increased free individual complexes. The presence of significant amounts of free CIV and CIII in
257 the absence of CL is sufficient to explain alterations in the kinetics of Cyt *c* transfer of electrons
258 between CIII/CIV as we previously demonstrated for mitochondria isolated from *crd1Δ* cells¹³.

259 An additional lipid stabilizing factor for SC formation appears to be anionic lipid nucleation
260 of lipid domains at the interface of CIII/CIV. The fatty acid hydrophobic tails of all the CLs are in
261 close proximity to side chains of hydrophobic amino acids and other phospholipids (PE and PC),
262 which further stabilizes these interactions. Although CDL402L and CDL601H appear not to lie
263 within the interface between CIV and CIII, the former is in close proximity to CDL302C
264 (Supplementary Fig. 5d and 6c), which in turn is in close proximity to CDL601K (Supplementary
265 Fig. 5c and d). CDL601K is the only CL that interacts with both CIII and CIV. Furthermore,
266 additional phospholipids (PE and PC) (Fig. 5a and b, left) are resolved in close association with
267 the above CLs at or close to the interface. Additional phospholipids most likely fill the empty
268 spaces between CIII and CIV, but might be too flexible to be resolved in the structure. Given that

269 reconstitution of the tetrameric SC from individual complexes *in vitro* only occurs when CL is
270 present ¹⁴ strongly suggests that CL nucleates a domain of phospholipids at the CIII/CIV interface
271 dependent on specific interactions of CL with SC protein components, thus further stabilizing SC
272 formation. As with CLs, the fatty acid hydrophobic tails of all the PGs are in close proximity to side
273 chains of hydrophobic amino acids and other phospholipids (PE and PC) (Fig. 5a and b, right),
274 which may also form a hydrophobic domain that further stabilizes the trimeric SC. However, the
275 hydrophobic space occupied by PG is considerably less than that of CL, which in turn lowers its
276 potential to stabilize hydrophobic interactions. As shown in the electrostatic potential map (Fig. 6)
277 of the WT tetrameric and *crd1Δ* trimeric SCs, the negatively charged headgroups of CL and PG,
278 respectively, are positioned in close association with a positively charged surface at the CIII/CIV
279 interface. In addition, more global hydrophobic interactions of CL molecules or PG molecules with
280 other phospholipids and amino acid side-chains are also significant contributors to the formation
281 of SCs (Fig. 5). Therefore, anionic phospholipids in conjunction with protein-protein interactions
282 are primary stabilizing forces for SC formation with CL being more stabilizing than PG.

283 The reduced stability of the PG-containing SC has important implications for human
284 respiratory SC organization in Barth Syndrome (BTHS) resulting from a mutation in the *TAZ1*
285 gene. SCs isolated from normal mammalian mitochondria, like those from yeast, are enriched in
286 CL over bulk mitochondrial CL ¹⁷. However, normal mammalian mitochondria, unlike yeast
287 mitochondria, contain detectable levels of PG, which are significantly elevated in BTHS along with
288 alterations in the CL pool fatty acid composition, reduced CL levels and increased lyso-CL ³⁹.
289 Most interestingly, SC stability is reduced in extracts from BTHS mitochondria when compared to
290 normal mitochondria extracts. In spite of differences in respiratory SC organization in mammalian
291 mitochondria, which also contains Complex I (CI), when compared to yeast SC organization,
292 CI/CIII SC and free CIV levels are elevated in BTHS mitochondrial extracts that display aberrant
293 CL and PG levels. The increased level of PG in BTHS might be expected to cause similar
294 destabilization of normal association of CIV with CIII in the CI/CIII/CIV SC. Therefore, the structure
295 and the lipid composition of respiratory complexes isolated from BTHS patients should be
296 investigated.

297

298 **Methods**

299 **Yeast strains and cell growth.** *S. cerevisiae* strain USY00b (*Mat α, ade2-1, his3-11-15, leu2-3-*
300 *112, trp1-1, ura3-52, can1R-100, atp2::LEU2, TRP1::ATP2-His₆*) expresses the F₀F₁-ATPase
301 subunit 2 with a C-terminal HIS₆ extension ⁴⁷. The strain was cultivated in growth medium
302 containing 1% yeast extract, 2% peptone, and 3.7% of lactic acid or 1% ethanol (v/v) and 3%

Figure 5.

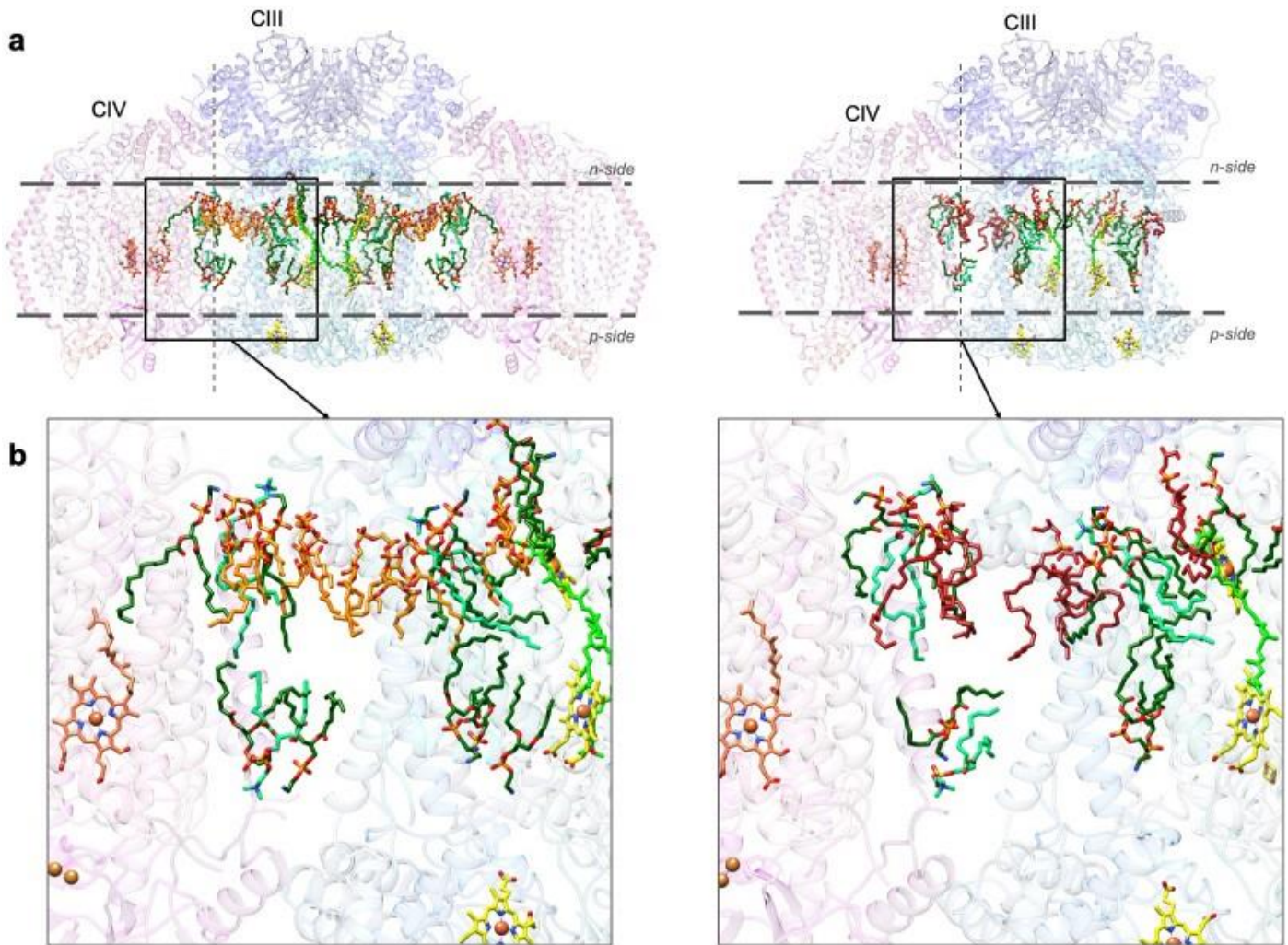


Figure 5. Location of identified lipids and cofactors. (a) An overview of the WT SC tetramer (left) and *crd1Δ* SC trimer (right) with lipids and cofactors colored by type. (b) A zoomed-in region reveals the lipid arrangement at the CIII/CIV interface; WT SC (left) and *crd1Δ* SC (right).

Figure 6.

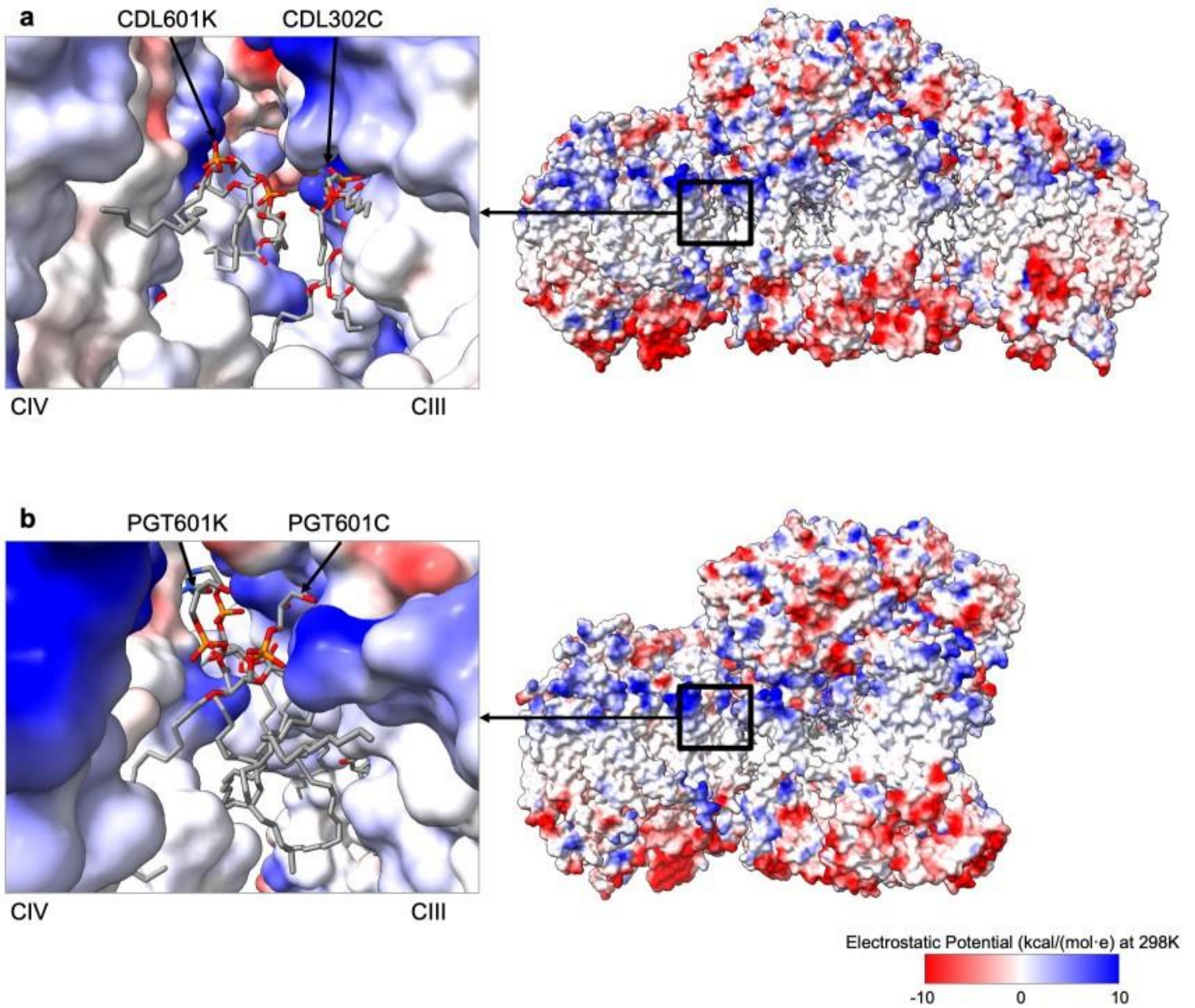


Figure 6. Electrostatic potential map of the WT SC and *crd1Δ* SC. Electrostatic potential map (generated in ChimeraX 50 based on Coulomb's law) is mapped onto the WT SC (a) and *crd1Δ* SC (b); (blue, positive charge and red, negative charge). The boxed-out region (on the left) reveals the electrostatic pocket at the CIV-CIII interface. The headgroups of CDL x 2 (a) and PGT x 2 (b) have complementary charges when compared to the interacting surface of the protein. The values mapped are in units of kcal/(mol·e) at 298° K.

303 glycerol at 30 °C. The cells were harvested (OD₆₀₀ of 2.0-3.0) by centrifugation and washed with
304 cold TBS buffer (50 mM Tris-HCl, pH 7.4 containing 150 mM NaCl) ⁹).

305 A *crd1*Δ strain (named YEB100) that encodes the Cox4p subunit of CIV with a 10-residue
306 His-tag at its C-terminus was constructed as follows. A complete replacement of the *CRD1*
307 gene (*crd1::KanMX4*) was isolated from a commercial strain (Horizon Discovery Ltd., catalog
308 #201935630) YSC6273 (*Mat a, his3 leu2 lys2 met15 trp1 ura3 crd1::KanMX4*) by PCR using
309 primers outside of the replaced *CRD1* gene. The isolate was used to transform a previously
310 constructed strain carrying the *COX4-His₁₀* gene (*Mata his3 leu2 ura3 COX4-His₁₀*) ¹⁴.
311 Transformants were selected for growth on YPD medium agar plates supplemented with 200
312 µg/ml G-418 antibiotic. The resulting strain (*Mata his3 leu2 ura3 crd1::KanMX4 COX4-His₁₀*) was
313 verified by PCR analysis for replacement of the *CRD1* gene by the *KanMX4* gene. The strain was
314 grown in 1% yeast extract, 2% peptone, 1% ethanol (v/v) and 3% glycerol at 30 °C. Cells were
315 harvested (OD₆₀₀ of 3.0) by centrifugation and washed with cold PBS buffer.

316

317 **Isolation of Mitochondria.** Mitochondria from WT and *crd1*Δ strains were isolated from
318 spheroplasts of yeast cells as previously described ¹³ except that 3 mg of Zymolase-20T per g of
319 cells were used, and incubation time was 90 min. Isolated mitochondria were further purified by
320 centrifugation at 30,000 rpm (SW41 Ti) at 4° C for 90 min through a density gradient containing
321 60%, 32%, 23% and 15% layers of sucrose in 15 mM Tris-HCl buffer, pH 7.4 and 20 mM KCl ⁹.
322 Mitochondria were either used immediately or flash-frozen with liquid N₂ and stored at -80°C.

323

324 **ESI-MS analysis of CD and PG.** Presence of the elevated level of PG in the CL synthase lacking
325 *crd1*Δ strain was confirmed by CL and PG molecular species quantification in mitoplast samples
326 by liquid chromatography (LC) coupled to electrospray ionization mass spectrometry (MS) in an
327 API 4000 mass spectrometer (Sciex, Framingham, MA) as previously described ²⁹. Lipid extracts
328 of mitoplasts from the *crd1*Δ mutant were loaded onto a LC/MS system with a CL internal standard
329 (1 µmole of tetramyristoyl-CL; Avanti Polar Lipids, Alabaster, AL) to verify the lack of CL and the
330 presence of PG (13.4 nmol/mg of mitoplast protein).

331

332 **Purification of SCs.**The III₂IV₂ SC from the CL-containing WT USY00b strain was purified as
333 previously described ⁹. Isolated mitochondria (8 mg of protein) were suspended in the 1 ml of lysis
334 buffer containing 2% (w/v) digitonin (Invitrogen), 50 mM potassium acetate, 10% glycerol, 1:50
335 volume protease inhibitor cocktail set III (Calbiochem), 1.5 mM phenylmethylsulfonyl fluoride and
336 30 mM HEPES-KOH, (pH 7.4) for 1h at 4°C with gentle shaking. After incubation the lysate was

337 centrifuged at 4° C for 20 min at 45,000 rpm (TLA55 rotor). 1 ml of supernatant was incubated
338 with 0.45 ml of magnetized Cobalt Beads (Dynabeads TALON catalog #101.02D, Invitrogen) for
339 45 min at 4° C with constant shaking to remove F₀F₁-ATPase. Prior to use, beads were washed
340 3 times with TBS using a magnetic separator (Magna-Sep™ Magnetic Particle Separator,
341 Invitrogen) to recover the beads. After incubation the beads were removed using a magnetic
342 separator. The supernatant (1 ml) was immediately layered onto an 8 ml sucrose gradient (0.75
343 M to 1.5 M sucrose in 15 mM Tris-HCl (pH 7.2), 20 mM KCl, and 0.4% digitonin) and centrifuged
344 at 4° C for 20 h at 30,000 rpm (TLS-55 swinging bucket rotor). Fractions (80-100 µL) from the
345 gradient were analyzed by BN-PAGE as previously described⁹. Selected fractions containing the
346 purified III₂IV₂ SC were combined and used for cryo-EM. Protein concentrations were determined
347 using the BCA protein assay kit (Thermo Scientific) according to manufacturer's instructions.

348 The III₂IV₁ trimeric SC from mitochondria of CL-lacking (*crd1Δ*) YEB100 strain was purified
349 as follows. Mitochondria were solubilized as described above. The clarified lysate was loaded at
350 1 ml/min onto a 5 ml His-Trap HP column (source Millipore Sigma) that was previously equilibrated
351 with 50 mM HEPES, 500 mM NaCl and 0.05% digitonin, pH 8.0 (Buffer B). The loaded column
352 was washed with several volumes Buffer B. Proteins were eluted with 20% of Buffer B containing
353 100 mM Imidazole. Fractions containing the highest absorbance at 280 nm were subjected to size
354 exclusion chromatography to separate the III₂IV₁ SC from contaminating individual CIII and CIV.
355 A Sepharose 6 column (GE) was pre-equilibrated with column buffer containing 50 mM Tris, 150
356 mM NaCl, 0.05% digitonin. The sample from the His-Trap column was loaded and eluted with
357 column buffer. Fractions were collected based on peak intensity at 280 nm. All fractions were
358 analyzed by BN-PAGE. Fractions containing the III₂IV₁ SC were pooled and used for cryo-EM.

359
360 **Western blot analysis and in-gel enzyme activity**-.BN-PAGE of purified SCs was performed in
361 3-12% acrylamide as described previously¹⁴. Gels were transferred for Western blot analysis to
362 a PVDF membrane. For CIII or CIV visualization polyclonal antibody (obtained from Cocalico
363 Biologicals) were used. Secondary antibody peroxidase-conjugated AffiniPure Goat anti-rabbit
364 and anti-Guinea pig IgG (H+L) from Jackson ImmunoResearch Laboratories, Inc. was used.
365 SuperSignal Western Femto Sensitivity kit (Thermo Scientific) was used to develop the signal
366 according to the manufacturer's instructions. The signal was captured by a Bio-Rad ChemiDoc
367 MP Imaging System.

368 For CIII in gel activity the purified protein samples were subjected to Colorless Native-PAGE
369 (CN-PAGE) as we described before¹⁴. The gel was incubated in the presence of 0.05% (w/v)
370 diaminobenzidine (DAB) in 50 mM potassium phosphate buffer (pH 7.2) for several h at room

371 temperature ⁴⁸. For CIV activity the purified protein samples were subjected to BN-PAGE. Gels
372 were incubated in the presence of horse heart Cyt c (0.05%, w/v) and 0.05% 3,3'-
373 Diaminobenzidine (w/v) in 50 mM phosphate buffer (pH 7.2) as described ¹⁴.

374 Although the in-gel assays are qualitative, CIV activity was robust while CIII activity was
375 weak for the *crd1Δ* SC when compared to the results previously observed for the WT SC ¹⁴. Since
376 both activities are comparable to WT activities when assayed in isolated mitochondria ¹³, low
377 activity of CIII isolated from *crd1Δ* cells is due to loss during purification.

378

379 **Grids preparation, cryo-EM data collection and image processing.** Grids for cryo-EM were
380 prepared as previously described ⁹. Data were collected with a Titan Krios microscope (Thermo
381 Fisher Scientific) operated at 300 kV (Supplementary Table 1). A post-GIF K2 Summit direct
382 electron detector (Gatan) operating in counting mode was used at a nominal magnification of
383 130,000x (pixel size of 1.07 Å) for image collection, and an energy slit with a width of 20 eV was
384 used during data collection. A total dose of 49 eV/Å² fractionated over 35 frames was employed.
385 Nominal defocus range set from -1.5 μm to -3.5 μm. Here, 20,253 micrograph movies were
386 collected during multiple imaging sessions under identical conditions.

387 The tetrameric SC was processed with CryoSPARC ⁴⁹. Patch motion was used for frame
388 alignment and exposure weighting with default parameters. Blob picker was initially used on a
389 subset of images (300) to select a subset of particles, which were then used to generate a low-
390 resolution template. Template particle picking was then performed and the resulting particles were
391 extracted using a 320 Å² box size. A total of 1,510,025 particles were selected. Multiple rounds
392 of 2D classification followed, narrowing the dataset to 834,191 particles and then to 413,626
393 particles. An initial refinement was completed using C1 symmetry, resulting in a 4.14 Å density
394 map. A non-uniform refinement followed by a local refinement with a tight mask further improved
395 the resolution to 3.4 Å. Finally, a large heterogeneous 3D classification refinement routine was
396 completed using four classes to sort the larger dataset (834,191 particles). These four initial
397 models (density maps) contained the 3.4 Å structure, a density map that was soft masked to only
398 contain CIII, another density map that was soft masked to contain CIII and a noisy CIV, and a
399 final map that appeared to only be noise. In total, 493,055 particles fell into the 3.4 Å map class.
400 A final refinement with a dynamic mask was performed resulting in a 3.2 Å final density map.

401 Samples of the purified trimeric SC (III₂IV₁) isolated from the *crd1Δ* strain were applied to
402 a 400-mesh copper grid containing ultrathin carbon support on lacey film that were glow
403 discharged at 30 mAmp for 15 sec. Grids containing samples were incubated at 100% humidity
404 (inside a Vitrobot (FEI) chamber) for 1 min, blotted for 3 s and rapidly frozen in liquid ethane using

405 a Vitrobot. Grids were stored at liquid nitrogen temperature for further analysis using cryo-EM.
406 The data collection was similar to that of the tetrameric SC described above. A total of 12,006
407 micrograph movies were collected. The *crd1Δ* dataset was imported with CryoSPARC and
408 evaluated manually, at which point the number of micrographs was trimmed down to 9,942
409 micrograph movies. Patch motion was used for frame alignment and exposure weighting with
410 default parameters. Blob picker was initially used to select particles on a subset of images (300),
411 which were then used to generate a low-resolution template. Template particle picking was then
412 performed and particles were extracted using a 320 Å² box size. An initial 1,926,302 particles
413 were selected by the template picker, and after multiple rounds of 2D classification, the data were
414 trimmed down to 638,401 particles. A strong presence of top and end-on views was visualized in
415 the 2D class averages, as was smearing of density in the 3D reconstructions, indicating preferred
416 orientation. When assessing particle orientations there were two distinct peaks in the data limiting
417 the resolution and resolvability in the maps. Due to preferred orientation, an additional 4,452
418 images were collected with a 30° tilt. This data was collected on a Titan Krios under similar
419 microscope conditions, aside from the tilt. The tilt data was again processed with CryoSPARC in
420 a similar fashion to the non-tilt data. Blob picker was used to select particles and after inspection
421 and extraction, 545,397 particles were obtained. Two rounds of 2D classification followed,
422 resulting in 186,312 particles being selected. The tilt data was then added to the previous dataset
423 to be processed in combination. A final heterogeneous refinement was performed on all the
424 particles (tilt + non-tilt data) similar to the WT. The class that had CIII and CIV best resolved had
425 745,670 particles. This dataset was further refined using a tight mask. The resulting map was
426 refined to 3.3 Å, improving upon the previous 3.5 Å map which did not include tilt data.
427 Resolvability also improved, specifically in CIV.

428

429 **Model Construction.** Construction of the tetrameric SC model (III₂IV₂) began by fitting the
430 previously reported structure of the III₂IV₂ mitochondrial respiratory supercomplex from *S.*
431 *cerevisiae* (6HU9)¹⁰. This model, which included all proteins of interest and some ligands, was
432 fitted into the tetrameric SC density map using the “Fit in Map” option in UCSF Chimera⁵⁰. Qcr9
433 needed an additional adjustment (rigid body rotation), which was made with Chimera. Geometry
434 minimization was run on the model to idealize the structure before refinement. Phenix real-space
435 refinement followed¹⁷ with ligand and Elbow restraints added and non-crystallographic symmetry
436 (NCS) constraints turned off (due to non-strict C2 symmetry) and metal linking turned on. To
437 optimize the CIII and CIV interface, subunit Cor1 of CIII and subunit Cox5a of CIV were submitted
438 to GalaxyRefineComplex⁵¹, a protein-protein complex refinement tool driven by interface

439 repacking, via Galaxy Web. The top 10 docks all contained similar interface statistics and each of
440 these models were fit to the density map and compared to the refined model. Docking 6 was
441 chosen as the top model as it had the best fit-to-density and no clashes with other CIII and CIV
442 subunits. This was then combined with the Phenix refined model.

443 Before iterating between real-space refinements and manual adjustments, PDB chains
444 were renamed to account for pseudosymmetry (see Supplementary Table 3). As noted during the
445 map reconstruction process, one CIV had less resolved density than the other, and thus the
446 iterative model refinement process was focused on the stronger CIV density side (denoted as the
447 reference-side). Throughout the modeling process, a trimer model consisting of the CIII (III₂) dimer
448 and one CIV on the reference-side was refined. Once refined, the opposite CIV was assessed
449 and modeled. Additional density was present in various regions of the map, with a majority in CIII.
450 To isolate this additional density, a difference map was created from the model. This difference
451 map revealed a noisy detergent band around the transmembrane portion of the supercomplex,
452 as well as discrete densities within CIII and at the interface of CIII and CIV. In an attempt to model
453 these densities, previously resolved yeast SCs and CIII (6YMX, 1KB9, 3CX5, 6Q9E, 6GIQ
454 ^{11,16,18,41,42}) were fit into the density map using Chimera. This excess density was modeled with
455 four UQ6 ligands, CN5 (CL) at the 2-fold of CIII, and CL in similar positions to 6YMX. Moreover,
456 excess density was found at the location where PE was modeled in 6YMX. This was renamed to
457 PEF, rigid-body fit with Chimera, and manually adjusted in COOT ⁵². Ligand restraints (.cif files)
458 were then generated in Phenix ⁴⁰ for ligands that were not defined in the Phenix ligand library.
459 Furthermore, Elbow restraints were computed using phenix.metal coordination, ensuring that
460 bonds with metal ions were maintained during model refinement. Finally, multiple iterations of
461 Phenix real-space refinement (using the above restraints and NCS symmetry turned off) and
462 COOT adjustments were done to improve the fit-to-density and model geometry of the trimer
463 complex. Throughout the refinements, ligands were manually altered to better fit the weaker
464 density. Once complete, the refined reference CIV model was duplicated and rigid-body-fit into
465 the opposite-side CIV density. An additional iteration of real-space refinement, without the aid of
466 NCS restraints, was run to improve fit-to-density and obtain B-factor values for the tetramer before
467 model interpretation (Supplementary Fig. 10).

468 Modeling of the *crd1Δ* density map began by independently fitting the optimized WT
469 protein subunits from CIII and CIV into the density map with Chimera. Iterative refinement of the
470 protein complex was performed using Phenix real-space refinement and COOT. Once complete,
471 the *crd1Δ* SC map was masked using the protein model to reveal unmodelled density. Hemes,
472 appropriate ligands (PEF, PCF) and cofactors were rigid-body fit to the unmodeled parts of the

473 *crd1Δ* SC density map. When analyzing the masked density and the corresponding model, it was
474 noted that the CDL locations did not have one-to-one matching density. The density at these
475 positions revealed two tails with one strong headgroup. Anionic phospholipid PGT, was then fit
476 into the CDL positions. Phenix was then used to generate ligand and metal bond restraints, and
477 real-space refinement followed. As with the WT, COOT and Phenix were iteratively used to
478 optimize the modeled complex. Ligand density that was disordered, specifically tail density was
479 truncated. For the chain/subunits names and ligands see Supplementary Table 4

480 To further analyze the PGT fitting, PEF, PCF, and CDL were all fit into the PGT density
481 locations using Chimera. One iteration of Phenix real-space refinement was completed with the
482 ligands in the isolated PGT density. A calculated density map was computed for each of the ligand
483 groups and the threshold was set to be equivalent for each ligand group. The cross-correlation
484 was computed for the six locations between the experimental masked density and the calculated
485 density (Supplementary Table 5)^{53,54} with PGT density showing the highest correlation.

486 For both the WT and *crd1Δ* structures, visualization and analysis of the final models was
487 done with UCSF Chimera, COOT, Phenix, and Molprobity⁵⁵. Moreover, LigPlot+⁵⁶ was used to
488 analyze the ligands at the CIV-CIII interface. Settings in LigPlot+ were changes such that
489 hydrogen bond D-A pairs had a maximum distance of 4 Å and non-bonded interacting residues
490 were only between hydrophobic-hydrophobic contacts.

491

492 **References**

493

- 494 1. Wenz T, Hielscher R, Hellwig P, Schagger H, Richers S, Hunte C. Role of phospholipids
495 in respiratory cytochrome *bc₁* complex catalysis and supercomplex formation. *Biochim*
496 *Biophys Acta* **1787**, 609-616 (2009).
497
- 498 2. Dudkina NV, Kouril R, Peters K, Braun HP, Boekema EJ. Structure and function of
499 mitochondrial supercomplexes. *Biochim Biophys Acta* **1797**, 664-670 (2010).
500
- 501 3. Lenaz G. Mitochondria and reactive oxygen species. Which role in physiology and
502 pathology? *Adv Exp Med Biol* **942**, 93-136 (2012).
503
- 504 4. Schagger H. Respiratory chain supercomplexes. *IUBMB Life* **52**, 119-128 (2001).
505
- 506 5. Stuart RA. Supercomplex organization of the oxidative phosphorylation enzymes in yeast
507 mitochondria. *J Bioenerg Biomembr* **40**, 411-417 (2008).
508
- 509 6. Wittig I, Schagger H. Supramolecular organization of ATP synthase and respiratory chain
510 in mitochondrial membranes. *Biochim Biophys Acta* **1787**, 672-680 (2009).
511

- 512 7. Acin-Perez R, Fernandez-Silva P, Peleato ML, Perez-Martos A, Enriquez JA. Respiratory
513 active mitochondrial supercomplexes. *Mol Cell* **32**, 529-539 (2008).
514
- 515 8. Maranzana E, Barbero G, Falasca AI, Lenaz G, Genova ML. Mitochondrial Respiratory
516 Supercomplex Association Limits Production of Reactive Oxygen Species from Complex
517 I. *Antioxid Redox Signal* **19**, 1469-1480 (2013).
518
- 519 9. Mileykovskaya E, Penczek PA, Fang J, Mallampalli VK, Sparagna GC, Dowhan W.
520 Arrangement of the respiratory chain complexes in *Saccharomyces cerevisiae*
521 supercomplex III₂IV₂ revealed by single particle cryo-electron microscopy. *J Biol Chem*
522 **287**, 23095-23103 (2012).
523
- 524 10. Hartley AM, *et al.* Structure of yeast cytochrome c oxidase in a supercomplex with
525 cytochrome bc1. *Nat Struct Mol Biol* **26**, 78-83 (2019).
526
- 527 11. Rathore S, *et al.* Cryo-EM structure of the yeast respiratory supercomplex. *Nat Struct Mol*
528 *Biol* **26**, 50-57 (2019).
529
- 530 12. Zhang M, Mileykovskaya E, Dowhan W. Gluing the respiratory chain together. Cardiolipin
531 is required for supercomplex formation in the inner mitochondrial membrane. *J Biol Chem*
532 **277**, 43553-43556 (2002).
533
- 534 13. Zhang M, Mileykovskaya E, Dowhan W. Cardiolipin is essential for organization of
535 complexes III and IV into a supercomplex in intact yeast mitochondria. *J Biol Chem* **280**,
536 29403-29408 (2005).
537
- 538 14. Bazán S, Mileykovskaya E, Mallampalli VK, Heacock P, Sparagna GC, Dowhan W.
539 Cardiolipin-dependent reconstitution of respiratory supercomplexes from purified
540 *Saccharomyces cerevisiae* complexes III and IV. *J Biol Chem* **288**, 401-411 (2013).
541
- 542 15. Hartley AM, Meunier B, Pinotsis N, Marechal A. Rcf2 revealed in cryo-EM structures of
543 hypoxic isoforms of mature mitochondrial III-IV supercomplexes. *Proc Natl Acad Sci U S*
544 *A* **117**, 9329-9337 (2020).
545
- 546 16. Berndtsson J, *et al.* Respiratory supercomplexes enhance electron transport by
547 decreasing cytochrome c diffusion distance. *EMBO Rep* **21**, e51015 (2020).
548
- 549 17. Althoff T, Mills DJ, Popot JL, Kuhlbrandt W. Arrangement of electron transport chain
550 components in bovine mitochondrial supercomplex I(1)III(2)IV(1). *Embo J* **30**, 4652-4664
551 (2011).
552
- 553 18. Letts JA, Fiedorczuk K, Degliesposti G, Skehel M, Sazanov LA. Structures of Respiratory
554 Supercomplex I+III₂ Reveal Functional and Conformational Crosstalk. *Mol Cell* **75**, 1131-
555 1146 e1136 (2019).
556
- 557 19. Wu M, Gu J, Guo R, Huang Y, Yang M. Structure of Mammalian Respiratory
558 Supercomplex I1III2IV1. *Cell* **167**, 1598-1609 e1510 (2016).
559
- 560 20. Gasanoff ES, Yaguzhinsky LS, Garab G. Cardiolipin, Non-Bilayer Structures and
561 Mitochondrial Bioenergetics: Relevance to Cardiovascular Disease. *Cells* **10**, (2021).
562

- 563 21. Paradies G, Petrosillo G, Paradies V, Ruggiero FM. Mitochondrial dysfunction in brain
564 aging: role of oxidative stress and cardiolipin. *Neurochem Int* **58**, 447-457 (2011).
565
- 566 22. Chicco AJ, Sparagna GC. Role of cardiolipin alterations in mitochondrial dysfunction and
567 disease. *American journal of physiology Cell physiology* **292**, C33-44 (2007).
568
- 569 23. Paradies G, Petrosillo G, Paradies V, Ruggiero FM. Role of cardiolipin peroxidation and
570 Ca²⁺ in mitochondrial dysfunction and disease. *Cell calcium* **45**, 643-650 (2009).
571
- 572 24. McMillin JB, Dowhan W. Cardiolipin and apoptosis. *Bioch Biophys Acta* **1585**, 95-107
573 (2002).
574
- 575 25. Huang Z, *et al.* Cardiolipin deficiency leads to decreased cardiolipin peroxidation and
576 increased resistance of cells to apoptosis. *Free Radic Biol Med* **44**, 1935-1944 (2008).
577
- 578 26. Ostrander DB, Sparagna GC, Amoscato AA, McMillin JB, Dowhan W. Decreased
579 cardiolipin synthesis corresponds with cytochrome *c* release in palmitate-induced
580 cardiomyocyte apoptosis. *J Biol Chem* **276**, 38061-38067 (2001).
581
- 582 27. Saini-Chohan HK, *et al.* Cardiolipin biosynthesis and remodeling enzymes are altered
583 during development of heart failure. *J Lipid Res* **50**, 1600-1608 (2009).
584
- 585 28. Sparagna GC, *et al.* Loss of cardiac tetralinoleoyl cardiolipin in human and experimental
586 heart failure. *J Lipid Res* **48**, 1559-1570 (2007).
587
- 588 29. Sparagna GC, Johnson CA, McCune SA, Moore RL, Murphy RC. Quantitation of
589 cardiolipin molecular species in spontaneously hypertensive heart failure rats using
590 electrospray ionization mass spectrometry. *J Lipid Res* **46**, 1196-1204 (2005).
591
- 592 30. Dumas JF, Peyta L, Couet C, Servais S. Implication of liver cardiolipins in mitochondrial
593 energy metabolism disorder in cancer cachexia. *Biochimie* **95**, 27-32 (2012).
594
- 595 31. McKenzie M, Lazarou M, Thorburn DR, Ryan MT. Mitochondrial respiratory chain
596 supercomplexes are destabilized in Barth Syndrome patients. *J Cell Biol* **361**, 462-469
597 (2006).
598
- 599 32. Paradies G, Paradies V, Ruggiero FM, Petrosillo G. Cardiolipin and mitochondrial function
600 in health and disease. *Antioxid Redox Signal* **20**, 1925-1953 (2014).
601
- 602 33. Antoun G, *et al.* Impaired mitochondrial oxidative phosphorylation and supercomplex
603 assembly in rectus abdominis muscle of diabetic obese individuals. *Diabetologia* **58**, 2861-
604 2866 (2015).
605
- 606 34. Gomez LA, Hagen TM. Age-related decline in mitochondrial bioenergetics: Does
607 supercomplex destabilization determine lower oxidative capacity and higher superoxide
608 production? *Semin Cell Dev Biol* **23**, 758-767 (2012).
609
- 610 35. Moe A, Di Trani J, Rubinstein JL, Brzezinski P. Cryo-EM structure and kinetics reveal
611 electron transfer by 2D diffusion of cytochrome *c* in the yeast III-IV respiratory
612 supercomplex. *Proc Natl Acad Sci U S A* **118**, (2021).
613

- 614 36. Chang SC, Heacock PN, Mileykovskaya E, Voelker DR, Dowhan W. Isolation and
615 characterization of the gene (*CLS1*) encoding cardiolipin synthase in *Saccharomyces*
616 *cerevisiae*. *J Biol Chem* **273**, 14933-14941 (1998).
617
- 618 37. Jiang F, *et al.* Absence of cardiolipin in the *crd1* null mutant results in decreased
619 mitochondrial membrane potential and reduced mitochondrial function. *J Biol Chem* **275**,
620 22387-22394 (2000).
621
- 622 38. Pfeiffer K, *et al.* Cardiolipin stabilizes respiratory chain supercomplexes. *J Biol Chem* **278**,
623 52873-52880 (2003).
624
- 625 39. Vreken P, *et al.* Defective remodeling of cardiolipin and phosphatidylglycerol in Barth
626 syndrome. *Biochem Biophys Res Commun* **279**, 378-382 (2000).
627
- 628 40. Liebschner D, *et al.* Macromolecular structure determination using X-rays, neutrons and
629 electrons: recent developments in Phenix. *Acta Crystallogr D Struct Biol* **75**, 861-877
630 (2019).
631
- 632 41. Lange C, Nett JH, Trumpower BL, Hunte C. Specific roles of protein-phospholipid
633 interactions in the yeast cytochrome *bc1* complex structure. *Embo J* **20**, 6591-6600
634 (2001).
635
- 636 42. Solmaz SR, Hunte C. Structure of complex III with bound cytochrome c in reduced state
637 and definition of a minimal core interface for electron transfer. *J Biol Chem* **283**, 17542-
638 17549 (2008).
639
- 640 43. Letts JA, Fiedorczuk K, Sazanov LA. The architecture of respiratory supercomplexes.
641 *Nature* **537**, 644-648 (2016).
642
- 643 44. Ostrander DB, Zhang M, Mileykovskaya E, Rho M, Dowhan W. Lack of mitochondrial
644 anionic phospholipids causes an inhibition of translation of protein components of the
645 electron transport chain. A yeast genetic model system for the study of anionic
646 phospholipid function in mitochondria. *J Biol Chem* **276**, 25262-25272 (2001).
647
- 648 45. Hunte C, Koepke J, Lange C, Rossmannith T, Michel H. Structure at 2.3 Å resolution of the
649 cytochrome *bc₁* complex from the yeast *Saccharomyces cerevisiae* co-crystallized with an
650 antibody Fv fragment. *Structure* **8**, 669-684 (2000).
651
- 652 46. Brzezinski P, Moe A, Adelroth P. Structure and Mechanism of Respiratory III-IV
653 Supercomplexes in Bioenergetic Membranes. *Chem Rev* **121**, 9644-9673 (2021).
654
- 655 47. Mueller DM, Puri N, Kabaleeswaran V, Terry C, Leslie AG, Walker JE. Ni-chelate-affinity
656 purification and crystallization of the yeast mitochondrial F1-ATPase. *Protein Expr Purif*
657 **37**, 479-485 (2004).
658
- 659 48. Wittig I, Karas M, Schagger H. High resolution clear native electrophoresis for in-gel
660 functional assays and fluorescence studies of membrane protein complexes. *Mol Cell*
661 *Proteomics* **6**, 1215-1225 (2007).
662
- 663 49. Punjani A, Rubinstein JL, Fleet DJ, Brubaker MA. cryoSPARC: algorithms for rapid
664 unsupervised cryo-EM structure determination. *Nature methods* **14**, 290-296 (2017).

- 665
666 50. Pettersen EF, *et al.* UCSF Chimera--a visualization system for exploratory research and
667 analysis. *J Comput Chem* **25**, 1605-1612 (2004).
668
669 51. Heo L, Lee H, Seok C. GalaxyRefineComplex: Refinement of protein-protein complex
670 model structures driven by interface repacking. *Sci Rep* **6**, 32153 (2016).
671
672 52. Emsley P, Cowtan K. Coot: model-building tools for molecular graphics. *Acta Crystallogr*
673 *D Biol Crystallogr* **60**, 2126-2132 (2004).
674
675 53. Vasishtan D, Topf M. Scoring functions for cryoEM density fitting. *J Struct Biol* **174**, 333-
676 343 (2011).
677
678 54. van Heel M, Schatz M, Orlova E. Correlation functions revisited. *Ultramicroscopy* **46**, 307-
679 316 (1992).
680
681 55. Chen VB, *et al.* MolProbity: all-atom structure validation for macromolecular
682 crystallography. *Acta Crystallogr D Biol Crystallogr* **66**, 12-21 (2010).
683
684 56. Laskowski RA, Swindells MB. LigPlot+: multiple ligand-protein interaction diagrams for
685 drug discovery. *J Chem Inf Model* **51**, 2778-2786 (2011).
686

687 **Acknowledgements**

688
689 This work was supported in part by NIH/NIGMS (R01GM115969) and the John S. Dunn Research
690 Foundation to W.D. and NIH/NIGMS (P01GM063210) to M.L.B.
691

692 **Author Contributions**

693
694 W.D and E.M. conceptualization and supervised the project and designed the research.
695 V.K.P.S.M. and E.I.B did sample preparation and biochemical analysis. V.K.P.S.M. and S.A. did
696 cryo-EM data collection. G.F., I.I.S. and S.A. did preliminary data processing. C.F.H. and M.L.B.
697 did final data processing and constructed the models. E.M, C.F.H., M.L.B and W.D. did structure
698 analysis and interpretation. G.C.S. did mass spectral analysis. E.M., W.D., C.F.H. and M.L.B
699 wrote the manuscript. I.I.S. provided important incite into the writing of the manuscript. All authors
700 provided information and/or critical comments during manuscript preparation. W.D
701 (william.dowhan@uth.tmc.edu) and E.M. (eugenia.mileykovskaya@uth.tmc.edu) are co-
702 corresponding authors.
703

704 **Competing information**

705 None for all authors

Supplementary Files

This is a list of supplementary files associated with this preprint. Click to download.

- [SupplementFilesFinal.pdf](#)